Magnetic Resonance Imaging 107 (2024) 88–99

Contents lists available at ScienceDirect

Magnetic Resonance Imaging

journal homepage: www.elsevier.com/locate/mri

Review Article

Amide proton transfer-weighted imaging of the abdomen: Current progress and future directions

Liuji Sheng [a,b,1], Enyu Yuan [a,b,1], Fang Yuan [a,*,2], Bin Song [a,b,c,*,2]

[a] Department of Radiology, West China Hospital, Sichuan University, Chengdu, Sichuan, China
[b] Functional and Molecular Imaging Key Laboratory of Sichuan Province, West China Hospital, Sichuan University, Chengdu, Sichuan, China
[c] Department of Radiology, Sanya People's Hospital, Sanya, Hainan, China

ARTICLE INFO

Keywords:
Magnetic resonance imaging
Chemical exchange saturation transfer
Amide proton transfer-weighted imaging
Abdominal application
State of the art

ABSTRACT

The chemical exchange saturation transfer technique serves as a valuable tool for generating in vivo image contrast based on the content of various proton groups, including amide protons, amine protons, and aliphatic protons. Among these, amide proton transfer-weighted (APTw) imaging has seen extensive development as a means to assess the biochemical status of lesions. The exchange from saturated amide protons to bulk water protons during and following the saturation ratio frequency pulse contributes to detectable APT signals. While APTw imaging has garnered significant attention in the central nervous system, demonstrating noteworthy findings in cerebral neoplasia, stroke, and Alzheimer's disease over the past decade, its application in the abdomen has been a relatively recent progression. Notably, studies have explored its utility in hepatocellular carcinoma, prostate cancer, and cervical carcinoma within the abdominal context. Despite these advancements, there is a paucity of reviews on APTw imaging in abdominal applications. This paper aims to fill this gap by providing a concise overview of the fundamental theories underpinning APTw imaging. Additionally, we systematically summarize its diverse clinical applications in the abdomen, with a particular focus on the digestive and urogenital systems. Finally, the manuscript concludes by discussing technical limitations and factors influencing APTw imaging in abdominal applications, along with prospects for future research.

1. Introduction

Amide proton transfer weighted (APTw) imaging is a type of molecular magnetic resonance imaging (MRI) technique derived from chemical exchange saturation transfer (CEST) imaging [1]. CEST, as a technique, leverages various proton groups within in vivo, including amide, amine, and aliphatic protons, to generate image contrast [2–5]. Due to the higher concentration of amide protons relative to other groups within in vivo, APTw imaging has developed the most extensively researched modality within the CEST framework [3].

The capability of APTw imaging lies in its indirect reflection of mobile proteins and peptides by facilitating asymmetry magnetization transfer from saturated amide protons to water protons, resulting to a measurable reduction in the water signal [1,2,6–10]. Moreover, APTw imaging adds value by capturing tissue physicochemical qualities, given that the exchange rate between amide protons and water protons is easily influenced by factors such as the potential of hydrogen (pH) [3,11]. While APTw imaging has garnered significant attention in cerebral applications, particularly in studies involving cerebral neoplasia, stroke, Alzheimer's disease, and Parkinson's disease [3,12–18], its introduction into abdominal imaging is a recent and promising development. Unlike brain imaging, which benefits from fewer motion

Abbreviation: ADC, apparent diffusion coefficient; APTw, amide proton transfer-weighted; AUC, area under the receiver operating curve; CEST, chemical exchange saturation transfer; CSC, cervical squamous carcinoma; D, true molecular diffusion coefficient; DKI, diffusion kurtosis imaging; DS, direct water saturation; DWI, diffusion weighted imaging; EA, endometrial adenocarcinoma; EC, endometrial carcinoma; HCC, hepatocellular carcinoma; IVIM, intravoxel incoherent motion imaging; MK, mean kurtosis; MRI, magnetic resonance imaging; MTC, magnetization transfer contrast; MTR_{asym}, asymmetry of magnetization transfer ration; PCa, prostate cancer; pH, potential of hydrogen; rNOE, nuclear Overhauser effect-relayed; 3D, three-dimensional.

* Corresponding authors at: Department of Radiology, West China Hospital, Sichuan University, No.37 Guoxue Alley, Chengdu 610041, Sichuan, China.
E-mail addresses: dr.yuan@foxmail.com (F. Yuan), songlab_radiology@163.com (B. Song).

[1] Liuji Sheng and Enyu Yuan contributed equally to this work.

[2] Fang Yuan and Bin Song co-supervised this work.

https://doi.org/10.1016/j.mri.2024.01.006
Received 17 October 2023; Received in revised form 13 January 2024; Accepted 14 January 2024
Available online 17 January 2024
0730-725X/

artifacts, minimal interference from fat, and a broader field of view, abdominal imaging encounters numerous challenges. Nevertheless, researchers have successfully applied APTw imaging to enhance the evaluation of abdominal diseases, achieving promising outcomes in liver lesions, prostate cancer (PCa), and cervical cancer [5,19–22]. To the best of our knowledge, a comprehensive overview of the state of research on abdominal applications using APTw imaging is notably absent in the literature. This review aims to bridge this gap by delving into the fundamentals of APTw imaging, providing a systematic summary of its applications in abdominal imaging (Fig. 1 and Table 1), and shedding light on the associated technical challenges and future prospects.

2. Principles and methods for APTw imaging

2.1. Basic principles

APTw imaging is a molecular imaging modality based on the CEST approach, the basic principle of which is shown in Fig. 2a. A two-pool exchanging model, consisting of a small solute pool from bound water and a large water pool from bulk water, forms the foundation of APTw imaging [23]. The saturation-labeled solute protons can transfer magnetization to unsaturated water when radiofrequencies are multi-irradiated with a resonance frequency corresponding to the particular solute protons. This process causes a drop in the immediately visible water signal, contributing to the minimal detectable concentration reaching toward micromolar levels [8,9]. Notably, the exchange rate of solute proton to water proton needs to be quick enough, and the spin lattice relaxation time of water needs to be sufficiently long [24]. Parts per million (ppm) is utilized to represent the offset from resonance frequency of free water proton to that of particular solute proton which can remain constant in various B_0 fields [5]. Numerous proteins and peptides at roughly the same frequency as amide protons can influence the assessment of amide group within in vivo MRI, leading to a large composite resonance achieving an overall proton concentration of about 50–100 mM [3].

2.2. APTw imaging acquisition

The CEST effects are often assessed by using the *Z*-spectrum, depicted in Fig. 2b as a function of irradiation frequency with $\frac{S_{sat}(\Delta\omega)}{S_0}$ using the bulk water resonant frequency as a zero-frequency reference. Here, S_0 represents the unsaturated water signal, and $S_{sat}(\Delta\omega)$ represents the water signal during saturation at a frequency offset of $\Delta\omega$ from the zero-frequency. An asymmetry analysis method of the *Z*-spectrum was proposed for mitigating the effect of direct water saturation (DS) and conventional semisolid magnetization transfer contrast (MTC) on in vivo APT imaging, as DS is symmetrical concerning the zero-frequency and MTC is symmetrical for the most part [25]. This approach employs the asymmetry of magnetization transfer ratio (MTR_{asym}) as a proxy of signal intensity across different proton groups, where MTR is the sum of all solute proton saturation effects at a specific frequency offset:

$$MTR(\Delta\omega) = 1 - \frac{S_{sat}(\Delta\omega)}{S_0}.$$

The APT effect of MTR asymmetry analysis is illustrated as follows, given the amide proton resonance frequency at an offset of 3.5 ppm [3]:

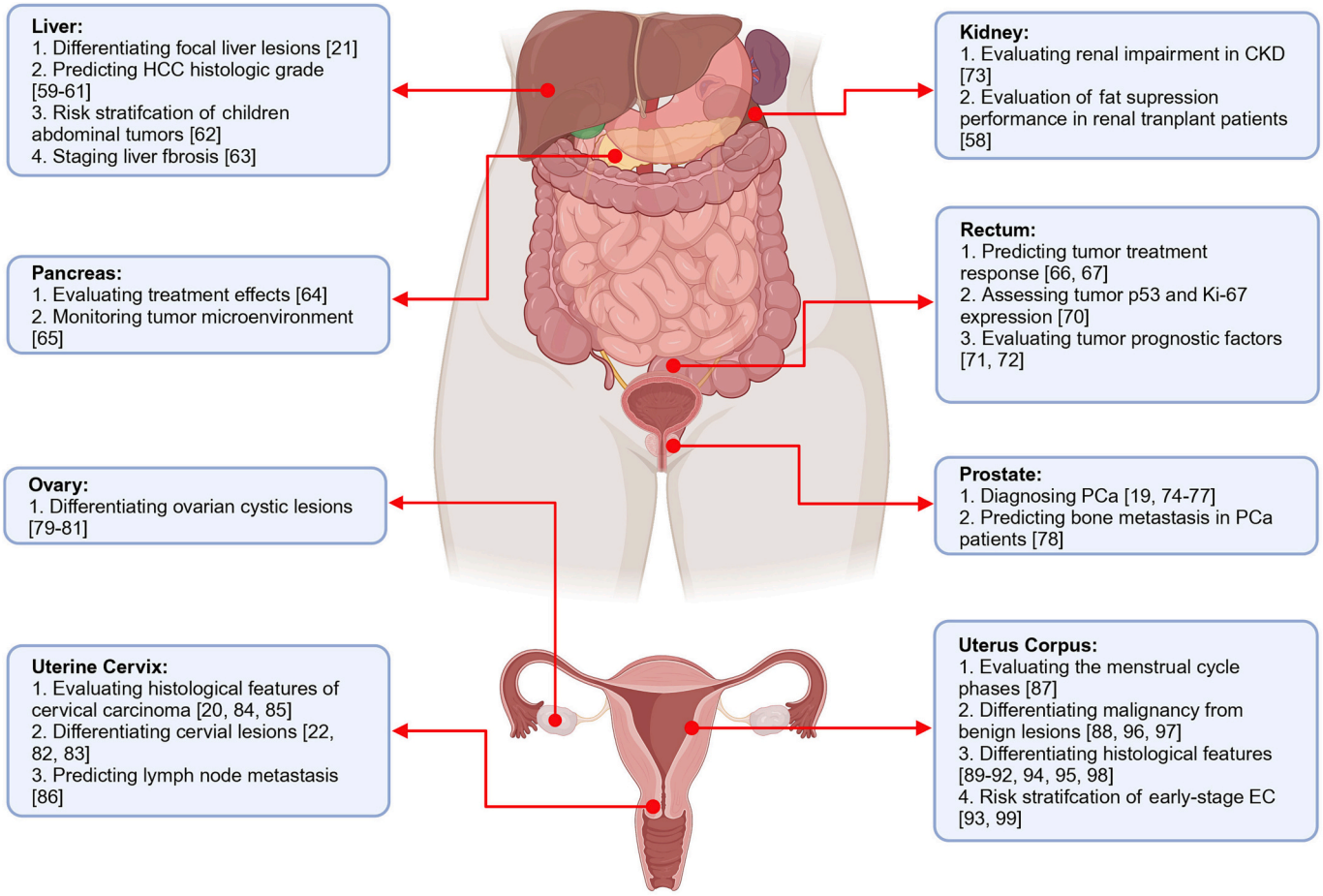

Fig. 1. The application of APTw imaging in the abdomen.

Table 1
Summary of selected APTw imaging studies in abdomen.

Reference	Publication year	Study design[a]	Population	Sample size	Task	AUC of APTw imaging
Liver						
Seo et al. [21]	2021	Retrospective	HCC, hemangioma, metastasis, cyst, ICC, FNH	79	Lesion differentiation	…
Wu et al. [59]	2020	Prospective	HCC	88	Histologic grade prediction	0.890 (0.805–0.947)
Lin et al. [60]	2019	Prospective	HCC	32	Histologic grade prediction	0.814 (0.637–0.929)
Wu et al. [61]	2020	Prospective	HCC	88	Histologic grade prediction	0.890 (0.805–0.947)
Jia et al. [62]	2022	Prospective	Pediatric abdominal tumors	57	Preoperative risk stratification	0.58–0.93
Lindquist et al. [63]	2021	Prospective	Male C57Bl/6 mice	8	Quantitative fibrosis estimation	…
Pancreas						
Maloney et al. [64]	2020	Prospective	PDA mice	18	pFUS treatment effects assessment	…
Vohra et al. [65]	2022	Prospective	Advanced PDA mice	24	Tumor micro-environment assessment	…
Rectum						
Nishie et al. [66]	2019	Retrospective	Locally advanced rectal adenocarcinoma	17	Treatment response prediction	0.87
Chen et al. [67]	2021	Retrospective	Locally advanced rectal adenocarcinoma	53	Treatment response prediction	0.824 (0.694–0.915)
Li et al. [70]	2020	Retrospective	Rectal adenocarcinoma	43	p53 and Ki-67 expression prediction	0.757–0.920
Chen et al. [71]	2021	Retrospective	Rectal adenocarcinoma	61	Pathologic features prediction	0.890 (0.784–0.956)
Li et al. [72]	2021	Retrospective	Rectal adenocarcinoma	110	Pathologic features prediction	0.737–0.921
Kidney						
Ju et al. [73]	2022	Prospective	Chronic kidney disease, healthy volunteers	55	Renal impairment evaluation	0.807–0.991
Stabinska et al. [58]	2022	Prospective	Renal transplant patients	14	Evaluation of fat suppression performance	…
Prostate						
Guo et al. [19]	2022	Prospective	PCa, BPH	140	Lesion differentiation	0.812 (0.735–0.888)
Yin et al. [74]	2021	Retrospective	PCa, BPH	100	Lesion differentiation	0.877 (0.832–0.968)
Jia et al. [75]	2011	Prospective	PCa	12	PCa and benign area differentiation	…
Yang et al. [76]	2023	Retrospective	PCa, BPH, prostatitis	79	Lesion differentiation	0.710–0.780
Qin et al. [77]	2023	Prospective	PCa	180	csPCa detection	0.878 (0.819–0.918)
Hu et al. [78]	2023	Retrospective	PCa	39	Bone metastasis prediction	0.719
Ovary						
Ishimatsu et al. [79]	2019	Prospective	Benign ovarian cystic lesions	18	Lesion differentiation	0.65–0.94
Li et al. [80]	2023	Retrospective	Ovarian cystic lesions	42	Lesion differentiation	0.910
Yu et al. [81]	2023	Retrospective	Ovarian masses with cystic components	46	Lesion differentiation	0.927–0.935
Uterine Cervix						
Meng et al. [20]	2020	Retrospective	CA, CSC	112	Pathological features differentiation	0.588–0.816
He et al. [22]	2019	Prospective	Cervical cancer, healthy volunteers	113	Cervical cancer and normal stroma differentiation	0.927
Li et al. [82]	2023	Prospective	CA, CSC	88	CSC and CA differentiation; high−/low-level CSC differentiation	0.708–0.731
Meng et al. [83]	2019	Retrospective	CA, CSC	76	CSC and CA differentiation; high−/low-level CSC differentiation	0.756 (0.609–0.904)
Li et al. [84]	2019	Prospective	CSC	31	Histologic grade prediction	0.848–0.876
Hou et al. [85]	2022	Prospective	CSC	46	Histologic grade prediction	0.871–0.883
Xu et al. [86]	2023	Retrospective	Cervical cancer	69	Lymph node metastasis prediction	0.763 (0.645–0.857)
Uterus Corpus						
Zhang et al. [87]	2019	Prospective	Healthy volunteers	20	Uterus signal intensities during the menstrual cycle	…

(*continued on next page*)

Table 1 (*continued*)

Reference	Publication year	Study design[a]	Population	Sample size	Task	AUC of APTw imaging
Li et al. [88]	2021	Prospective	EA, leiomyoma, adenomyosis, healthy volunteers	125	Lesion differentiation	0.870–0.905
Li et al. [89]	2021	Prospective	Stage I EC	22	Ki-67 expression prediction	0.768
Tian S, et al. [90]	2023	Retrospective	EC	47	p53 abnormal and p53 wild-type EC differentiation	0.739
Li et al. [91]	2023	Retrospective	EC	54	Her-2 Gene Expression	0.824 (0.696–0.914)
Li et al. [92]	2021	Prospective	EA	35	dMMR and pMMR tumor differentiation	0.778
Meng et al. [93]	2021	Prospective	Stage I EC	80	Preoperative risk stratification	0.768 (0.660–0.855)
Fu et al. [94]	2022	Prospective	EA	90	Histologic grade prediction; Ki-67 expression prediction	0.782 (0.683–0.862)
Ochiai et al. [95]	2022	Prospective	EC	33	Type I and type II EC differentiation	0.826 (0.667–0.985)
Tian et al. [96]	2023	Retrospective	EC, endometrial polyp	32	Stage Ia EC and endometrial polyp differentiation	0.850 (0.719–0.936)
Meng et al. [97]	2023	Retrospective	EC, endometrial polyp	53	Stage I-II EC and endometrial polyp differentiation	0.798
Ma et al. [98]	2022	Retrospective	EC	34	Microsatellite instability prediction	0.894
Jin et al. [99]	2022	Retrospective	Stage I EC	72	Risk factors prediction	0.748–0.828

Abbreviation: APTw: amide proton transfer-weighted; AUC: areas under the receiver operating curve; ICC: intrahepatic cholangiocarcinoma; FNH: focal nodular hyperplasia; PDA: pancreatic ductal adenocarcinoma; pFUS: pulsed focused ultrasound; HCC: hepatocellular carcinoma; PCa: prostate cancer; csPCa: clinically significant prostate cancer; BPH: benign prostatic hyperplasia; CA: cervical adenocarcinoma; CSC: cervical squamous carcinoma; EA: endometrial adenocarcinoma; EC: endometrial carcinoma; Her-2: human epidermal growth factor receptor-2; dMMR: mismatch repair deficiency; pMMR: mismatch repair proficient; EEA: endometrioid endometrial adenocarcinoma.

[a] All studies were single center.

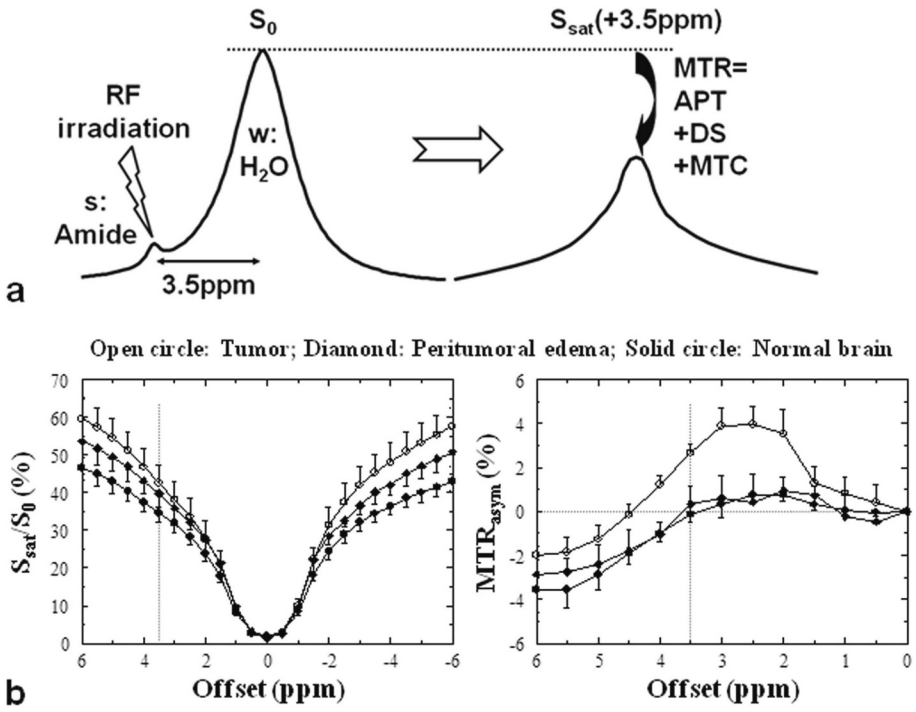

Fig. 2. a: CEST/APT detection enhancement principle. The small pool (s) reflects dilute exchangeable amide protons (at ~ 3.5 ppm downfield of the water resonance) of mobile proteins, and the large pool (w) reflects bulk water protons. The radiofrequency irradiation selectively saturates/labels exchangeable protons in pool s, which subsequently exchange with unsaturated protons of pool w (rate k_{sw}). b: Z-spectra and MTRasym spectra for tumor, peritumoral edema, and contralateral normal brain tissue in a 9 L tumor rat brain model (n = 5). Compared with the peritumoral edema and contralateral normal brain tissue regions, there is a substantial increase in the tumor MTRasym over the 2–3.5 ppm offset range. Reproduced with permission from Zhou et al, Magn Reson Med 2003;50:1120–1126 and Zhou et al, J Magn Reson Imaging 2019;50:347–364.

$$MTR_{asym}(3.5\ ppm) = MTR(3.5\ ppm) - MTR(-3.5\ ppm) = \frac{S_{sat}\ (-3.5\ ppm) - S_{sat}\ (3.5\ ppm)}{S_0} = APTR + MTR_{asym}'(3.5\ ppm),$$

where *APTR* denotes the amide proton transfer ratio, namely pure APT signals [23]. The term "APTw imaging" was suggested by Zhou et al. [26] to replace "APT imaging" due to the representation of composite resonance effects at around 3.5 ppm other than *APTR* by

$MTR_{asym}{}'(3.5\,ppm)$. The nuclear Overhauser effect-relayed (rNOE) exchange of aliphatic proton (at −3.5 ppm) is primarily responsible for the contributions of $MTR_{asym}{}'(3.5\,ppm)$ [27–30] and the MTC effect's inherent asymmetries [31]. Furthermore, a number of methods have recently emerged for extracting pure APT signals, including multi-pool Lorentzian fitting [32,33], voxel-wise optimization of pseudo-Voigt profile [34] and MTR_{Rex} [35].

2.3. Challenges in abdominal APTw imaging

APTw imaging, the sole commercial CEST imaging protocol on 3 Tesla MR scanners, has been used in about half of the investigations for the quantitative measurements of amide protons resonance effect [15]. However, this technique meets several inherent and unresolved issues in abdomen, such as time consuming and susceptibility to inhomogeneous B_0 and B_1. In addition, motion artifacts and fat interference due to the rNOE exchange effect are also notable. However, it is exciting to see that some workable solutions have been put out with persistent effort.

Currently, there are two main ways to shorten scan time of APTw imaging. Firstly, APTw imaging can be combined with certain traditional fast imaging techniques, such as gradient- and spin-echo and turbo-spin-echo [36,37]. Secondly, decreasing the number of k-space acquisitions is also a promising way that can be implemented by techniques such as variably-accelerated sensitivity encoding, spectroscopy with linear algebraic modeling, recurrent feature sharing reconstruction network and so on [38–45]. Nevertheless, the actual acquisition time reduction and special variant noise amplification in parallel imaging need to be solved [38].

Since APTw imaging acquisition and quantitative analysis are highly sensitive to B_0 and B_1, corrections for B_0 and B_1 are imperative. The B_0

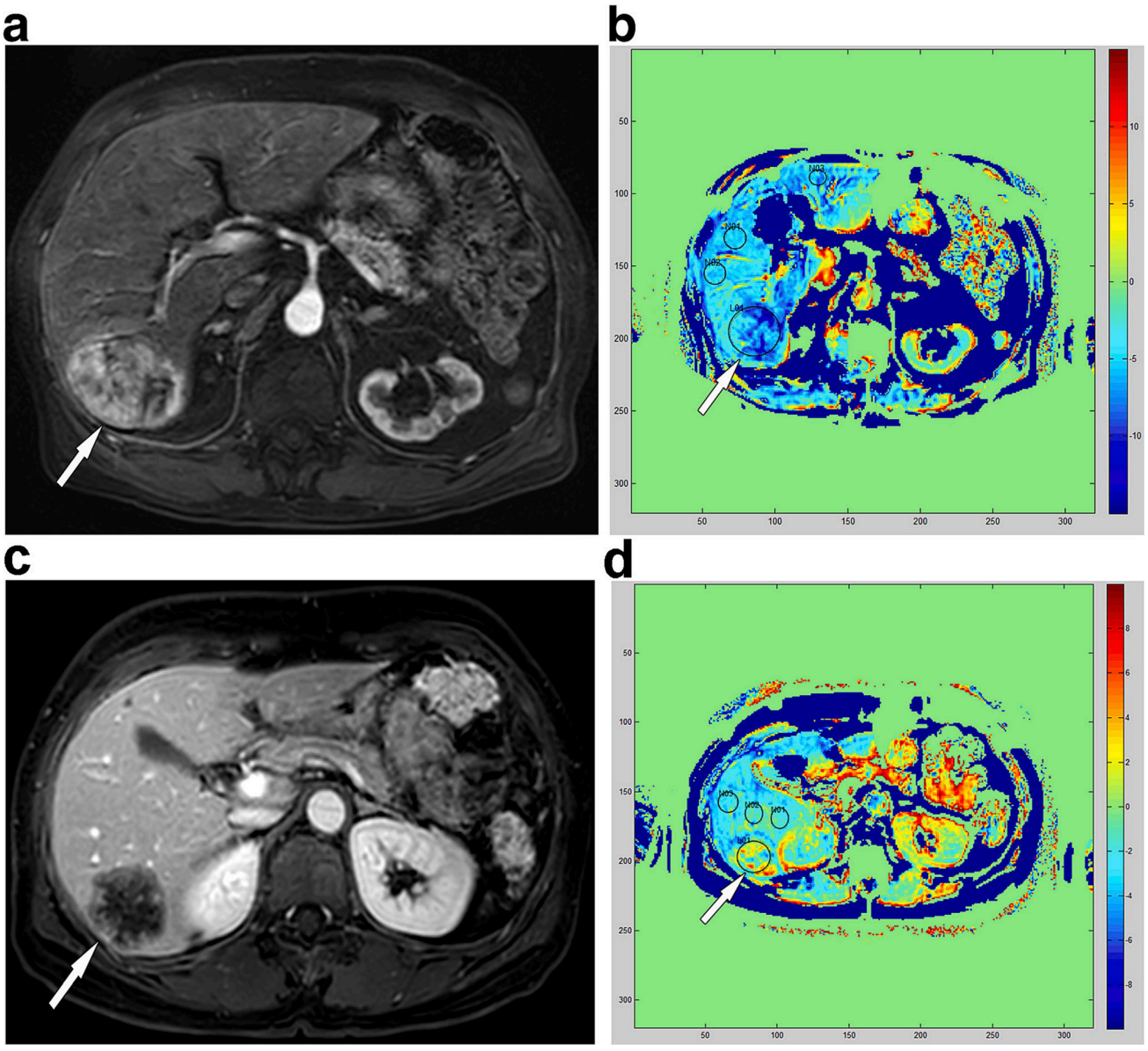

Fig. 3. Amide proton transfer weighted (APTw) imaging in a 78-year-old man with a hepatocellular carcinoma (HCC) and in a 61-year-old woman with hepatic metastases from colon cancer. a: Contrast-enhanced T1-weighed image obtained during the late arterial phase shows a 6.6-cm HCC (arrow) in the liver segment 6. b: On the corresponding APTw map, the magnetization transfer ratio asymmetry (MTR_{asym}) values of HCC and the background liver were − 7.23% and − 5.42%, respectively. c: Contrast-enhanced T1-weighed image obtained during the portal venous phase shows a 4.2-cm metastasis (arrow) in the liver segment 6. d: The corresponding APTw map shows an elevated MTR_{asym} value for metastasis (0.42%) than the averaged MTR_{asym} of three region of interests in the background liver (−1.98%). Reproduced with permission from Seo et al., Eur Radiol 2020; 31: 222–231.

shift map could be obtained through various methods, including the use of frequency-stabilized CEST imaging sequence [46], CEST-Dixon imaging sequence [47] fitted from a water saturation shift referencing method [48] or the interpolated *Z*-spectra, or employing three-dimensional (3D) fast spin-echo Dixon APTw imaging with self-generated B_0 [49]. Corrections for B_1 can be achieved through several methods, such as the Bloch-Siegert shift method [50], simultaneous mapping of water shift and B_1 [51], and other innovation techniques [52–56].

Fast image readout method was employed in abdominal APTw imaging in order to reduce motion-relation artifacts, such as echo planar imaging and fast imaging with steady-state precession [15]. Even though non-geometry-specific 3D saturation pulse can help amide protons saturation process without much motion effect, the water readout is significantly impacted. Utilizing volumetric navigators proves beneficial for real-time motion correction in CEST [57]. Eventually, it's worth noting that respiratory triggering and holding breath are still essential for minimizing motion-relation artifacts in clinical settings. When it comes to fat interference, the most popular techniques for fat suppression are chemical shift-based techniques, like frequency-specific excitation pulses for water imaging and CEST-Dixon imaging sequences conducting water-fat separation and B_0 mapping [47,58].

3. Application of APTw imaging in abdomen

3.1. APTw imaging in digestive system

3.1.1. Liver

Recent investigations have delved into the application of APTw imaging in liver studies, revealing valuable insights. Seo et al. explored the feasibility of liver APTw imaging and its efficacy in characterizing focal liver lesions across 203 patients [21]. Their findings demonstrated that liver metastasis exhibited higher APTw value than hepatocellular carcinoma (HCC) (Fig. 3). Notably, technical success was achieved in only 62.1% of the scans.

Beyond lesion characterization, APTw imaging emerges as a promising tool for predicting the histological grade of HCC. Several studies compared the APTw imaging with diffusion weighted imaging (DWI), diffusion kurtosis imaging (DKI) and intravoxel incoherent motion imaging (IVIM), and evaluated the diagnostic accuracy of APTw values against various parameters [59–61]. Results revealed the area under the receiver operating characteristic curves (AUC) for APTw values (AUC = 0.814–0.890) significantly surpassed DKI- and IVIM-derived parameters (AUC = 0.713–0.765) and marginally exceeded DWI-derived parameters (AUC = 0.745). In a study by Jia et al. [62] enrolled 57 children with abdominal tumors, APTw values successfully differentiated high-risk from low-risk neuroblastoma patients, but proved infeasible for distinguishing Wilms' tumors and hepatoblastomas patients.

Exploring the realm of liver fibrosis, Lindquist et al. [63] investigated the relationship between APTw values and the degree of fibrosis in a mouse model induced by CCl_4 administration. In vivo experiments demonstrated a modest correlation between the APTw values and histological results (r = 0.5–0.55), highlighting its potential value for noninvasive detection of chronic liver disease and potential staging. Nonetheless, further research in humans is imperative to validate and extend these promising findings.

3.1.2. Pancreas

As of now, the assessment of pancreatic states within the human body through APTw imaging remains an unexplored frontier, with only two relevant animal studies to date. Maloney et al. observed a significant enhancement in mean MTR and APTw values in genetically modified $Kras^{LSL\text{-}G12D/+}$, $Trp53^{LSL\text{-}R172H/+}$, Cre mouse models with pancreatic ductal cancer following pulsed focused ultrasound treatment [64]. In a separate study, Vohra et al. utilized quantitative multi-parametric 14 Tesla MRI to assess the tumor microenvironment in $Kras^{LSL\text{-}G12D/+}$, $Trp53^{LSL\text{-}R172H/+}$, Cre mouse models with advanced pancreatic ductal adenocarcinomas [65]. Their findings revealed a moderate association between tumor volume and glycosaminoglycan-CEST (r = 0.51) and MTR (r = 0.60), albeit not with APTw values (r = 0.28). In summary, while APTw imaging and the CEST technique exhibit potential for assessing therapeutic efficacy and tumor microenvironments, further investigations in human subjects are imperative to validate and expand upon these promising insights.

3.1.3. Rectum

For the prediction of neoadjuvant chemoradiotherapy response in patients with locally advanced rectal cancer, Nishie et al. observed that the APTw value in the low-response group was significantly higher than that in the high-response group [66]. In addition, the results of the study by Chen et al. demonstrated combining pre-treatment APTw and apparent diffusion coefficient (ADC) values resulted in significantly improved diagnostic performance compared to ADC values alone [67]. Notably, APTw imaging offers advantages over DWI as it is sensitive to the mucin and the acidic extracellular pH in rectal cancer, factors influencing the response of neoadjuvant chemoradiotherapy [66,68,69], and exhibits high reproducibility due to its higher spatial resolution compared to DWI.

In the pursuit of diagnostic and prognostic biomarkers, Li et al. [70] found that the APT mean signal intensity had superior diagnostic ability compared to the ADC mean in predicting different p53 and Ki-67 status of rectal adenocarcinoma (AUC = 0.757 and 0.920, respectively). A prospective study by Chen and colleagues, involving 61 patients with rectal adenocarcinoma undergoing 3D APTw imaging, indicated a significant positive correlation between mean APTw values and WHO grades (r = 0.550) [71]. Furthermore, mean APTw values exhibited the best performance, with 92.31% sensitivity and 79.17% specificity, for identifying low-grade and high-grade rectal adenocarcinoma compared to other image biomarkers. Another study by Li et al. [72] revealed significantly higher APTw values in WHO high-grade rectal adenocarcinoma compared to the low-grade group (2.668 ± 0.638% vs. 2.226 ± 0.347%). Furthermore, they observed a significant difference in APTw values between mucinous adenocarcinoma and common adenocarcinoma (3.192 ± 0.661% vs. 2.333 ± 0.471%). In conclusion, APTw imaging exhibits promising potential in predicting pathological prognosis-affecting characteristics and treatment response in rectal tumors. However, further research is essential to validate its accuracy in predicting recurrence and overall survival.

3.2. APTw imaging in Genito-urinary system

3.2.1. Kidney

The application of APTw imaging in kidney diseases is still in its infancy. Ju et al. examined the use of APTw imaging in evaluating renal function, involving 30 chronic kidney disease patients and 25 healthy volunteers [73]. Their findings indicated that cortical and medullary APTw values increased with worsening renal impairment, and the APTw values in the right renal cortex and medulla significantly correlated negatively with glomerular filtration rate (r = −0.80 and − 0.83). Additionally, Stabinska et al. validated the performance of two-point Dixon-based CEST imaging for fat suppression in an egg-phantom and 14 renal transplant recipients [58]. This method demonstrated the ability to obtain more accurate quantification of the APTw signal in the transplanted kidney patients. These observations suggested that APTw imaging holds promise as a novel method for non-invasively assessing renal function and impairment in the future.

3.2.2. Prostate

In the realm of PCa diagnosis and correlation with the Gleason Score, Yin et al. conducted a study enrolling 49 PCa patients and 51 patients with benign prostatic hyperplasia [74]. Their results demonstrated that the APTw value effectively distinguished PCa from benign prostatic

hyperplasia, achieving an AUC of 0.877. Moreover, it exhibited a moderate correlation with the Gleason score ($r = 0.640$). Another study by Guo et al. [19] (Fig. 4) revealed significant differences in APTw values among stromal, hyperplastic, and cancerous areas in the prostate. The APTw value (OR = 12.18) and 1/ADC (OR = 703.87) were independent predictors for distinguishing transition zone PCa from benign prostatic hyperplasia. Consistent findings in other studies further supported APTw imaging's efficacy, with AUCs ranging from 0.710 to 0.780 for differentiating PCa from benign prostate lesions [75,76]. Moreover, Qin et al. demonstrated the ability of APTw imaging to differentiate PCa grades with a sensitivity of 61.1% and specificity of 81.0% [77]. Expanding its utility, APTw imaging showed promise in predicting bone metastasis of PCa. The APTw value was significantly higher in the bone metastasis-positive group than in the bone metastasis-negative group (median = 2.65 vs. 2.48) [78].

3.2.3. Ovary

To evaluate the potential of APTw imaging for discriminating between various benign ovarian cystic lesions with different pre-saturated pulse durations, Ishimatsu et al. [79] gathered 19 observations from 18 patients. Notably, when pre-saturated pulse duration was 2.0 s, serous cystadenoma, mucinous cystadenoma and functional cyst exhibited significant differences, suggesting that APTw imaging might provide an early diagnosis of ovarian cystic lesions with the longer pre-saturation pulse. In a study by Li et al. involving 42 patients, the value of APTw imaging in identifying ovarian endometriotic cysts from other ovarian cystic lesions was assessed [80]. The results indicated that APTw imaging demonstrated excellent diagnostic efficacy in distinguishing ovarian endometriotic cysts from other ovarian cystic lesions, achieving an impressive AUC of 0.910. Additionally, Yu et al. also investigated the performance of APTw imaging in the differentiation between benign and malignant ovarian masses with cystic components. Their findings

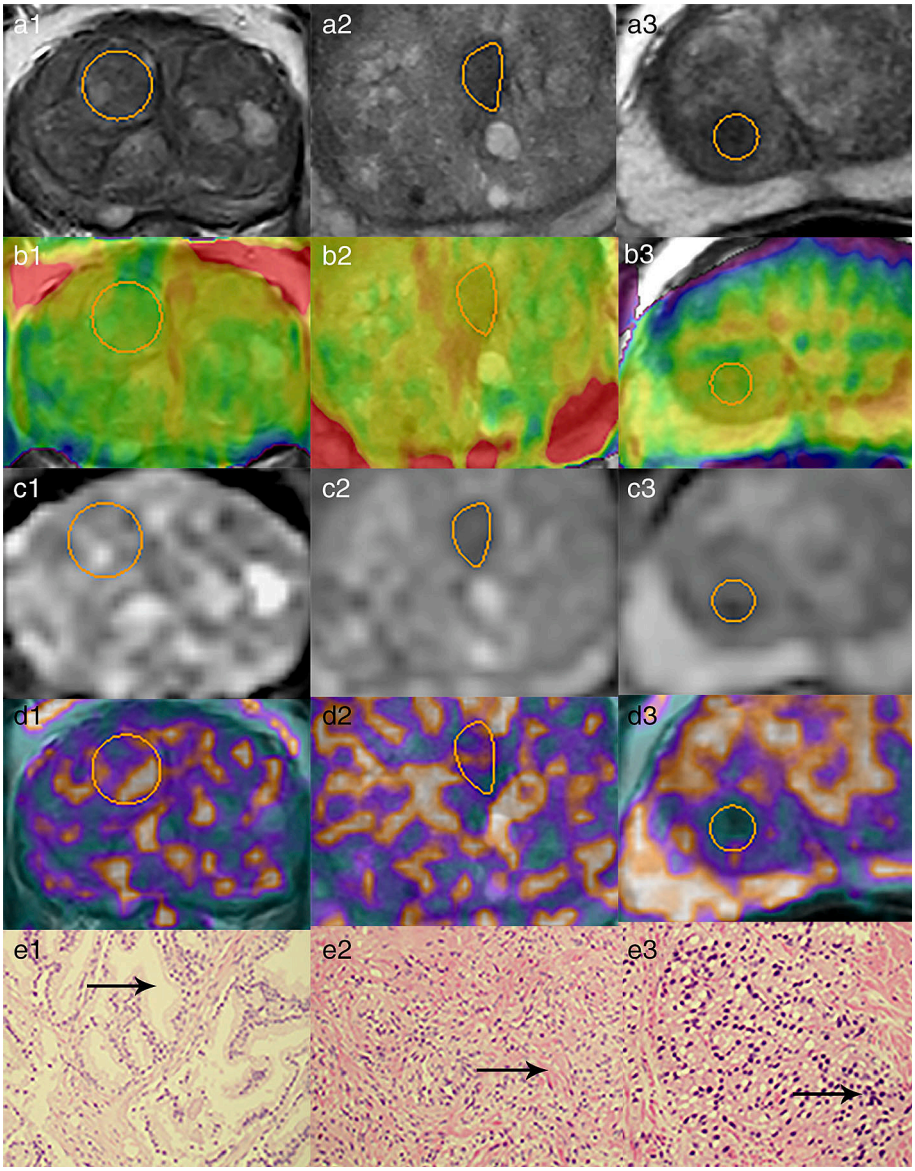

Fig. 4. Examples of the definition of the regions of interest (orange circle) for quantitative analyses. Row (a): T2WI image, row (b): APTw image with T2WI overlay, row (c): ADC image, row (d): T2*-weighted image with T2WI overlay, row (e): corresponding pathological pictures (magnification = 200) with the main pathologic features were marked (arrow). 1(a–e), glandular benign prostatic hyperplasia. Lesion appeared hyperintense on T2WI, APTw = 2.40%, ADC = 1.03×10^{-3} mm^2/s, T2* = 56.48 msec. 2(a–e), stromal benign prostatic hyperplasia. Lesion appeared hypointense on T2WI, APTw = 2.90%, ADC = 0.82×10^{-3} mm^2/s, T2* = 44.78 msec. 3(a–e), transition zone prostate cancer. Lesion appeared hypointense on T2WI, APTw = 3.20%, ADC = 0.77×10^{-3} mm^2/s, T2* = 39.64 msec. Reproduced with permission from Guo Z et al, J Magn Reson Imaging 2022; 56:1311–19.

revealed significant differences in APTw values of cystic regions between the two groups [81].

3.2.4. Uterine cervix

In the realm of cervical cancer detection, He et al. conducted an analysis of APTw images from 49 healthy individuals and 52 patients with cervical lesions [22]. Their findings demonstrated the majority of cases had good APTw image quality and the APTw imaging effectively differentiated cervical cancer from normal cervical stroma, with an AUC of 0.927. Subsequent studies [20,82,83] utilizing the APTw value showed moderate to good diagnostic performance in differentiating cervical adenocarcinoma and squamous cell carcinoma (AUC = 0.708–0.799). Notably, Meng et al. [20] reported that mean kurtosis (MK) exhibited superior performance (AUC = 0.882) compared to the APTw value (Fig. 5), a trend also observed in Li's study [82]. The Prediction of the pathological grade of cervical squamous cell carcinoma was a subject of extensive investigation [20,22,82–85]. These studies collectively found that the APTw value could differentiate low-grade and high-grade tumor with moderate to good performance (AUC = 0.731–0.883). Hou et al. [85] demonstrated the combination of APTw imaging, DWI and DKI was the most efficient method for identifying different grades in their study. Regarding the prediction of lymph node metastasis in cervical cancer, Xu et al. [86] observed APTw imaging demonstrated effective ability in identifying positive and negative lymph node metastasis, achieving an AUC of 0.763. However, predicting the International Federation of Gynecology and Obstetrics stage was

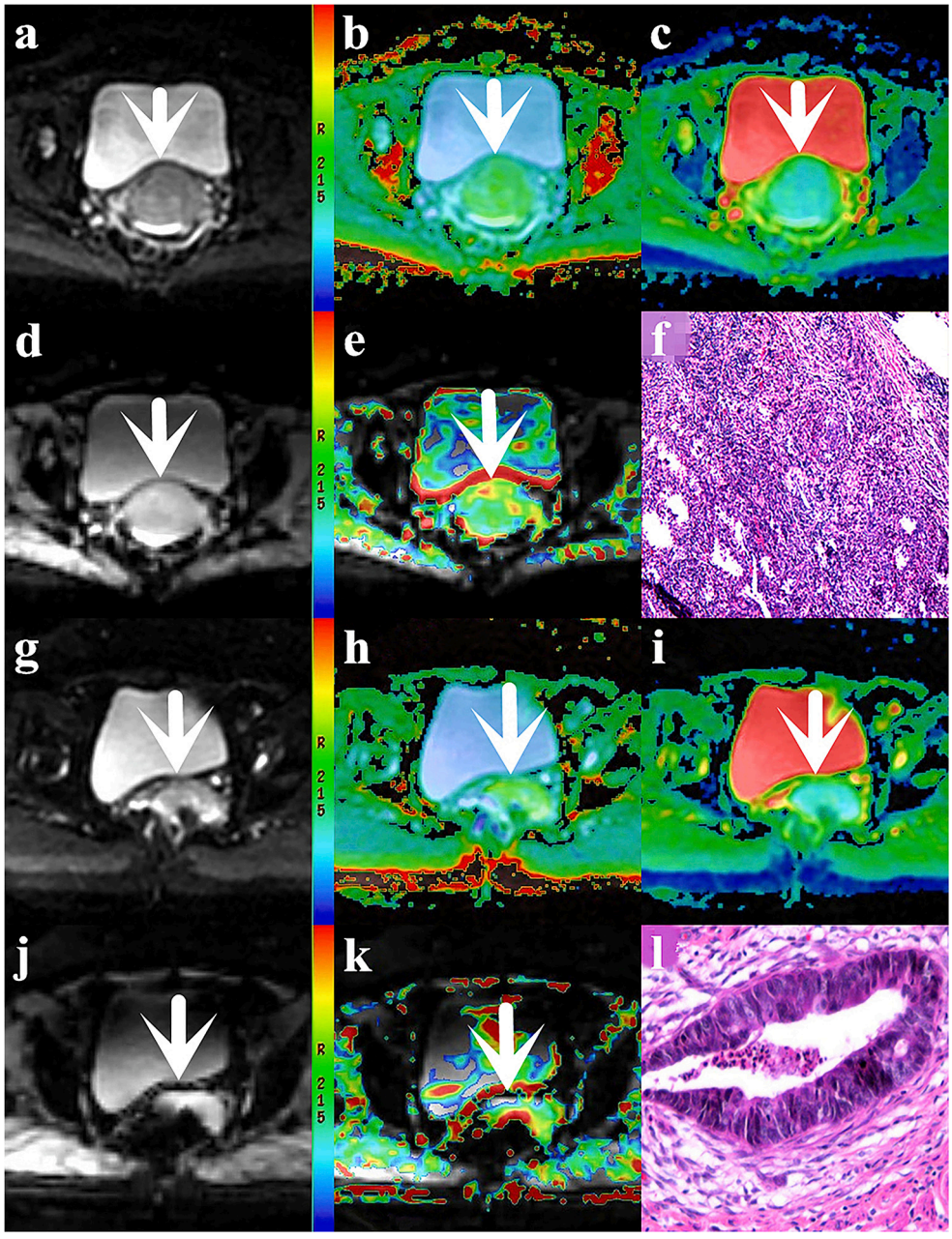

Fig. 5. (a–f) Female, 55 years, with staging IV, G3 CSC, apparent kurtosis coefficient = 0.943, non-Gaussian diffusion coefficient = 0.832 × 10^{-3} mm^2/s, MTR_{asym} (3.5 ppm) = 3.39%; (g–l) female, 66 years, with staging IB,G2 cervical adenocarcinoma, apparent kurtosis coefficient = 0.721, non-Gaussian diffusion coefficient = 1.06 × 10^{-3} mm^2/s, MTR_{asym} (3.5 ppm) = 3.16%. In these images, (a/g) are DKI original images, (b/h) are apparent kurtosis coefficient pseudocolored maps, (c/i) are non-Gaussian diffusion coefficient pseudo-colored maps, (d/j) are APTw imaging original images, (e/k) are MTR_{asym} (3.5 ppm) pseudocolored maps, and (f/l) are pathological images. Reproduced with permission from Meng et al., Eur Radiol 2020; 30: 5758–5767.

relatively difficult in current studies. The result of Meng et al. [20] revealed the MK was superior to the APTw value in differentiating advanced- and early-stage cervical cancer (AUC = 0.671 and 0.588, respectively). These findings collectively underscore the potential of APTw imaging as a valuable tool in various aspects of cervical cancer diagnosis and prognosis.

3.2.5. Uterus corpus

In the realm of abdominal studies utilizing APTw imaging, endometrial diseases have emerged as a pivotal focus. Zhang et al. [87] uncovered that APTw values exhibit variation in correlation with the menstrual cycle in healthy women of childbearing age.

Moreover, Li et al. observed significantly higher APTw values in endometrial adenocarcinoma (EA) compared to leiomyoma, adenomyosis and normal uterine myometrium [88]. This finding suggests that APTw imaging holds promise as a potential image biomarker for detecting and characterizing endometrial lesions. In a related study, Li et al. compared the capabilities of APTw imaging and IVIM for differentiating Ki-67 proliferation status in type I EC. APTw values of the high-proliferated Ki-67 group were significantly higher compared to the low-proliferated Ki-67, whereas no difference was observed using IVIM [89]. Analyzing 46 EC patient data, Tian et al. demonstrated APTw imaging could differentiate p53 abnormal from p53 wild-type EC, achieving an AUC of 0.739 [90]. Furthermore, Li et al. [91] utilized APTw imaging to estimate human epidermal growth factor receptor-2 expression in EC, concluding that it could be used to preoperatively assess the human epidermal growth factor receptor-2 expression (AUC = 0.824), contributing to more precise clinical treatment. APTw imaging and DWI were employed by Li et al. to evaluate the differences between mismatch repair deficient and proficient tumors in EA [92]. The APTw value was significantly higher in the deficient group than in the proficient group, while no significant differences were observed in ADC values. Meng et al. prospectively evaluated risk stratification in early-stage EC using APTw imaging and multiple DWI models [93]. They found that the low-risk group exhibited significantly lower perfusion fraction, MK and APTw values. The combination of APTw value, true molecular diffusion coefficient (D) and MK distinguished between low- and non-low-risk groups better than any single parameter (AUC = 0.958). Fu et al. discovered that APTw value and D were independent predictors for differentiating low- and high-grade EA, with a combined AUC (APTw value + D) of 0.892 [94]. Ochiai et al. [95] discovered that the maximum APTw value could differentiate type I and II EC, with an AUC of 0.826. For identifying early-stage EC and endometrial polyps, Tian et al. [96] and Meng et al. [97] found APTw imaging to be a valuable tool, with AUCs ranging from 0.798 to 0.850. Ma et al. demonstrated that combination of APTw value and pseudo-diffusion coefficient achieved the best diagnostic performance (AUC = 0.973), surpassing the individual parameter for differentiating microsatellite stabilization and instability groups [98]. Additionally, Jin et al. identified APTw value, mean diffusivity, and MK as independent risk predictors for stage I EC [99]. The combination of all these parameters yielded the best performance, reaching an AUC of 0.906, a sensitivity of 71.0%, and a specificity of 92.7%. These cumulative findings underscore the diverse applications and diagnostic potential of APTw imaging in the landscape of uterine corpus diseases.

4. Difficulties and future prospects of APTw imaging

Despite the promising results demonstrated in abdominal studies utilizing APTw imaging, several challenges persist, necessitating resolution. These challenges include ambiguity in interpreting results, lengthy scan time, correction for B_0 and B_1 inhomogeneity, and the elimination of artifacts.

4.1. Interpretability of results

Although it is well established that some aggressive tumors exhibit hyperintense and some ischemic tissues exhibit hypointense on APTw images, the interpretation of these images cannot solely be attributed to the concentration of mobile proteins and peptides or the low pH. Notably, the absence of uniform standards across vendors and guidelines for abdominal APTw imaging has led to variations in observed APTw values among studies, resulting in contradictory outcomes. Furthermore, the APTw signal is influenced by numerous components beyond the desired APT signal, complicating result interpretation. The impact of contributions from both the downfield and upfield sides of the *Z*-spectrum adds to the complexity. To address this challenge, practical techniques have been proposed for extracting the pure APT signal, including multi-pool Lorentzian fitting [32,33] and other techniques [34,35]. In summary, the urgent establishment of standardized criteria for APTw imaging across diverse tissues and organs is imperative to enhance the consistency and reliability of interpretation. This standardization will contribute significantly to the clarity and comparability of APTw imaging results in abdominal studies.

4.2. Time consuming

The protracted duration of APTw imaging poses a significant challenge for its clinical utility, prompting a need for comprehensive investigations into time reduction strategies. Two principal avenues have been explored to curtail scan time: by incorporating traditional fast imaging techniques and by decreasing the number of k-space acquisitions during the APTw imaging process. A recent advancement in this realm is the introduction of a quick and segmented 3D echo-planar imaging with incoherent undersampling in k-space 3D steady-state CEST MRI [43]. This innovative approach employs model-based reconstruction and spectral analysis to predict missing signals and CEST-specific spectral images collaboratively, mitigating the need for complete observations and thus reducing acquisition time. Another strategy involves a fast acquisition technique that combined the multiple interleaved mode saturation with fast online-customized parallel transmission excitation pulses and B_{1+} correction. This method aims to swiftly obtain homogeneous whole-brain coverage, enhancing the efficiency of the imaging process [44]. Additionally, a novel approach based on periodically rotated overlapping parallel lines enhanced reconstruction acquisition and deep neural network has been proposed to shorten acquisition time [45].

4.3. The inhomogeneity of B_0 and B_1

Due to a wider field of view and more diverse tissue composition in body imaging compared to brain imaging, the inhomogeneous problems of B_0 and B_1 are more difficult to solve. The APTw value's sensitivity to variations in B0 and B1 fields exacerbates the challenges in maintaining imaging quality. B_0 inhomogeneity, impacting the position of bulk water resonance, introduces complexities in APTw imaging, ultimately causing potential inaccuracies in APTw value measurements. Concerning the B_1 field, the MTC asymmetry within tissues significantly influences the APTw value at low B_1 fields. Conversely, the APT effect dominates at high B_1 fields [15,100]. This diversity in B_1 fields complicates the interpretation of APTw imaging, as the APTw value is influenced differently under varying B_1 conditions. A noteworthy observation by Zhou et al. [100] indicated that, despite significant differences in signal origin across studies conducted at different B_1 fields, the discrepancy of APTw values between malignancies and normal tissue remain consistent, with some academics evaluating that the outcomes of APTw imaging was a coincidental symbiotic effect [2].

4.4. Artifacts

The potential sources of artifacts in abdominal imaging are more varied than those in brain imaging, including interference from fat or air, physiological organ movement during imaging (such as normal breathing, and intestine peristalsis) and even errors brought by menstruation [87]. The broader field of view utilized in abdominal imaging amplifies the risk of B_0 inhomogeneity, further compromising image quality and increasing the likelihood of artifact generation. While some techniques for artifact removal have been mentioned earlier, there remains a need for enhanced methods with improved usability and correction efficacy.

5. Conclusion

In conclusion, APTw imaging, an evolution of CEST molecular MRI technology, generates image contrast based on amide protons in endogenous tissue, eliminating the need for external contrast agents. Despite notable achievements, the applications of APTw imaging in abdomen is relatively limited, with only a handful of studies surpassing 100 participants. Several challenges impede APTw imaging's clinical efficacy in abdominal applications, including issues related to imaging interpretability, extended scan times, artifacts, and the inhomogeneity of B_0 and B_1 fields. Addressing these challenges demands further exploration, emphasizing sequence optimization, standardized interpretation criteria, and promoting multi-center studies to enhance reproducibility and reliability in abdominal imaging. Consequently, APTw imaging holds significant promise as a clinical solution across various abdominal applications, provided these challenges are systematically addressed and overcome through continued research and development efforts.

CRediT authorship contribution statement

Liuji Sheng: Conceptualization, Data curation, Software, Visualization, Writing – original draft, Investigation. **Enyu Yuan:** Conceptualization, Data curation, Writing – review & editing, Investigation. **Fang Yuan:** Funding acquisition, Resources, Supervision, Writing – review & editing. **Bin Song:** Conceptualization, Funding acquisition, Project administration, Resources, Supervision, Writing – review & editing.

Declaration of competing interest

None.

Acknowledgements

Funding: This study was supported by the Research Grant of National Natural Science Foundation of China (Grant number U22A20343), Science and Technology Support Program of Sichuan Province (Grant number 2021YFS0021), Science and Technology Support Program of Sichuan Province (Grant number 2022YFQ0095), The 1.3.5 project for disciplines of excellence, West China Hospital, Sichuan University (Grant number ZYJC21012) and the 1.3.5 project for disciplines of excellence, West China Hospital, Sichuan University (Grant number ZYGD22004).

References

[1] Zhou J, Zaiss M, Knutsson L, Sun PZ, Ahn SS, Aime S, et al. Review and consensus recommendations on clinical APT-weighted imaging approaches at 3T: application to brain tumors. Magn Reson Med 2022;88(2):546–74.
[2] van Zijl PCM, Lam WW, Xu J, Knutsson L, Stanisz GJ. Magnetization transfer contrast and chemical exchange saturation transfer MRI. Features and analysis of the field-dependent saturation spectrum. NeuroImage 2018;168:222–41.
[3] Zhou J, Payen JF, Wilson DA, Traystman RJ, van Zijl PC. Using the amide proton signals of intracellular proteins and peptides to detect pH effects in MRI. Nat Med 2003;9(8):1085–90.
[4] Jin T, Wang P, Zong X, Kim SG. Magnetic resonance imaging of the amine-proton EXchange (APEX) dependent contrast. NeuroImage 2012;59(2):1218–27.
[5] Gao T, Zou C, Li Y, Jiang Z, Tang X, Song X. A brief history and future prospects of CEST MRI in clinical non-brain tumor imaging. Int J Mol Sci 2021;22(21).
[6] Zhou J, Zijl V. Chemical exchange saturation transfer imaging and spectroscopy. Prog Nucl Magn Reson Spectrosc 2006;48(2–3):109–36.
[7] Vinogradov E, Sherry AD, Lenkinski RE. CEST: from basic principles to applications, challenges and opportunities. J Magn Reson (San Diego, Calif: 1997) 2013;229:155–72.
[8] Sherry AD, Woods M. Chemical exchange saturation transfer contrast agents for magnetic resonance imaging. Annu Rev Biomed Eng 2008;10:391–411.
[9] Kogan F, Hariharan H, Reddy R. Chemical exchange saturation transfer (CEST) imaging: description of technique and potential clinical applications. Curr Radiol Rep 2013;1(2):102–14.
[10] Jones KM, Pollard AC, Pagel MD. Clinical applications of chemical exchange saturation transfer (CEST) MRI. J Magn Reson Imaging 2018;47(1):11–27.
[11] Pavuluri K, McMahon MT. pH imaging using chemical exchange saturation transfer (CEST) MRI. Israel J Chem 2017;57(9):862–79.
[12] Zhou J, Lal B, Wilson DA, Laterra J, van Zijl PC. Amide proton transfer (APT) contrast for imaging of brain tumors. Magn Reson Med 2003;50(6):1120–6.
[13] Salhotra A, Lal B, Laterra J, Sun PZ, van Zijl PC, Zhou J. Amide proton transfer imaging of 9L gliosarcoma and human glioblastoma xenografts. NMR Biomed 2008;21(5):489–97.
[14] Wang R, Li SY, Chen M, Zhou JY, Peng DT, Zhang C, et al. Amide proton transfer magnetic resonance imaging of Alzheimer's disease at 3.0 tesla: a preliminary study. Chin Med J (Engl) 2015;128(5):615–9.
[15] Zhou J, Heo HY, Knutsson L, van Zijl PCM, Jiang S. APT-weighted MRI: techniques, current neuro applications, and challenging issues. J Magn Reson Imaging 2019;50(2):347–64.
[16] Li C, Wang R, Chen H, Su W, Li S, Zhao X, et al. Chemical exchange saturation transfer MR imaging is superior to diffusion-tensor imaging in the diagnosis and severity evaluation of Parkinson's disease: a study on substantia Nigra and striatum. Front Aging Neurosci 2015;7:198.
[17] Li C, Peng S, Wang R, Chen H, Su W, Zhao X, et al. Chemical exchange saturation transfer MR imaging of Parkinson's disease at 3 tesla. Eur Radiol 2014;24(10):2631–9.
[18] Sun PZ, Zhou J, Sun W, Huang J, van Zijl PC. Detection of the ischemic penumbra using pH-weighted MRI. J Cerebral Blood Flow Metab 2007;27(6):1129–36.
[19] Guo Z, Qin X, Mu R, Lv J, Meng Z, Zheng W, et al. Amide proton transfer could provide more accurate lesion characterization in the transition zone of the prostate. J Magn Reson Imaging 2022;56:1311–9.
[20] Meng N, Wang X, Sun J, Han D, Ma X, Wang K, et al. Application of the amide proton transfer-weighted imaging and diffusion kurtosis imaging in the study of cervical cancer. Eur Radiol 2020;30(10):5758–67.
[21] Seo N, Jeong HK, Choi JY, Park MS, Kim MJ, Chung YE. Liver MRI with amide proton transfer imaging: feasibility and accuracy for the characterization of focal liver lesions. Eur Radiol 2021;31(1):222–31.
[22] He YL, Li Y, Lin CY, Qi YF, Wang X, Zhou HL, et al. Three-dimensional turbo-spin-echo amide proton transfer-weighted mri for cervical cancer: a preliminary study. J Magn Reson Imaging 2019;50(4):1318–25.
[23] Zhou J, Wilson DA, Sun PZ, Klaus JA, Van Zijl PC. Quantitative description of proton exchange processes between water and endogenous and exogenous agents for WEX, CEST, and APT experiments. Magn Reson Med 2004;51(5):945–52.
[24] Sun PZ, Wang E, Cheung JS, Zhang X, Benner T, Sorensen AG. Simulation and optimization of pulsed radio frequency irradiation scheme for chemical exchange saturation transfer (CEST) MRI-demonstration of pH-weighted pulsed-amide proton CEST MRI in an animal model of acute cerebral ischemia. Magn Reson Med 2011;66(4):1042–8.
[25] Guivel-Scharen V, Sinnwell T, Wolff SD, Balaban RS. Detection of proton chemical exchange between metabolites and water in biological tissues. J Magn Reson 1998;133(1):36–45 (San Diego, Calif : 1997).
[26] Zhou J, Blakeley JO, Hua J, Kim M, Laterra J, Pomper MG, et al. Practical data acquisition method for human brain tumor amide proton transfer (APT) imaging. Magn Reson Med 2008;60(4):842–9.
[27] Ling W, Regatte RR, Navon G, Jerschow A. Assessment of glycosaminoglycan concentration in vivo by chemical exchange-dependent saturation transfer (gagCEST). Proc Natl Acad Sci U S A 2008;105(7):2266–70.
[28] van Zijl PC, Yadav NN. Chemical exchange saturation transfer (CEST): what is in a name and what isn't? Magn Reson Med 2011;65(4):927–48.
[29] Jones CK, Huang A, Xu J, Edden RA, Schär M, Hua J, et al. Nuclear Overhauser enhancement (NOE) imaging in the human brain at 7T. NeuroImage 2013;77:114–24.
[30] Lu J, Zhou J, Cai C, Cai S, Chen Z. Observation of true and pseudo NOE signals using CEST-MRI and CEST-MRS sequences with and without lipid suppression. Magn Reson Med 2015;73(4):1615–22.
[31] Hua J, Jones CK, Blakeley J, Smith SA, van Zijl PC, Zhou J. Quantitative description of the asymmetry in magnetization transfer effects around the water resonance in the human brain. Magn Reson Med 2007;58(4):786–93.
[32] Zhou IY, Lu D, Ji Y, Wu L, Wang E, Cheung JS, et al. Determination of multipool contributions to endogenous amide proton transfer effects in global ischemia with high spectral resolution in vivo chemical exchange saturation transfer MRI. Magn Reson Med 2019;81(1):645–52.
[33] Wu Y, Zhou IY, Lu D, Manderville E, Lo EH, Zheng H, et al. pH-sensitive amide proton transfer effect dominates the magnetization transfer asymmetry contrast during acute ischemia-quantification of multipool contribution to in vivo CEST MRI. Magn Reson Med 2018;79(3):1602–8.

[34] Zhang L, Zhao Y, Chen Y, Bie C, Liang Y, He X, et al. Voxel-wise optimization of Pseudo Voigt profile (VOPVP) for Z-spectra fitting in chemical exchange saturation transfer (CEST) MRI. Quant Imaging Med Surg 2019;9(10):1714–30.
[35] Zaiss M, Bachert P. Chemical exchange saturation transfer (CEST) and MR Z-spectroscopy in vivo: a review of theoretical approaches and methods. Phys Med Biol 2013;58(22):R221–69.
[36] Zhu H, Jones CK, van Zijl PC, Barker PB, Zhou J. Fast 3D chemical exchange saturation transfer (CEST) imaging of the human brain. Magn Reson Med 2010;64 (3):638–44.
[37] Zhao X, Wen Z, Zhang G, Huang F, Lu S, Wang X, et al. Three-dimensional turbo-spin-echo amide proton transfer MR imaging at 3-tesla and its application to high-grade human brain tumors. Mol Imaging Biol 2013;15(1):114–22.
[38] Heo HY, Zhang Y, Lee DH, Jiang S, Zhao X, Zhou J. Accelerating chemical exchange saturation transfer (CEST) MRI by combining compressed sensing and sensitivity encoding techniques. Magn Reson Med 2017;77(2):779–86.
[39] Kujawa A, Kim M, Demetriou E, Anemone A, Livio Longo D, Zaiss M, et al. Assessment of a clinically feasible Bayesian fitting algorithm using a simplified description of chemical exchange saturation transfer (CEST) imaging. J Magn Reson (San Diego, Calif: 1997) 2019;300:120–34.
[40] Zhang Y, Heo HY, Jiang S, Zhou J, Bottomley PA. Fast 3D chemical exchange saturation transfer imaging with variably-accelerated sensitivity encoding (vSENSE). Magn Reson Med 2019;82(6):2046–61.
[41] Zhang Y, Heo HY, Jiang S, Lee DH, Bottomley PA, Zhou J. Highly accelerated chemical exchange saturation transfer (CEST) measurements with linear algebraic modeling. Magn Reson Med 2016;76(1):136–44.
[42] Wang P, Guo P, Lu J, Zhou J, Jiang S, Patel VM. Improving amide proton transfer-weighted MRI reconstruction using T2-weighted images. In: Medical Image Computing and Computer-Assisted Intervention: MICCAI International Conference on Medical Image Computing and Computer-Assisted Intervention. 12262; 2020. p. 3–12.
[43] Lee H, Choi SH, Sohn CH, Kim SG, Lee J, Park J. Rapid three-dimensional steady-state chemical exchange saturation transfer magnetic resonance imaging. Magn Reson Med 2021;85(3):1209–21.
[44] Liebert A, Tkotz K, Herrler J, Linz P, Mennecke A, German A, et al. Whole-brain quantitative CEST MRI at 7T using parallel transmission methods and B1+ correction. Magn Reson Med 2021;86(1):346–62.
[45] Guo C, Wu J, Rosenberg JT, Roussel T, Cai S, Cai C. Fast chemical exchange saturation transfer imaging based on PROPELLER acquisition and deep neural network reconstruction. Magn Reson Med 2020;84(6):3192–205.
[46] Liu R, Zhang H, Niu W, Lai C, Ding Q, Chen W, et al. Improved chemical exchange saturation transfer imaging with real-time frequency drift correction. Magn Reson Med 2019;81(5):2915–23.
[47] Zhang S, Seiler S, Wang X, Madhuranthakam AJ, Keupp J, Knippa EE, et al. CEST-Dixon for human breast lesion characterization at 3 T: a preliminary study. Magn Reson Med 2018;80(3):895–903.
[48] Kim M, Gillen J, Landman BA, Zhou J, van Zijl PC. Water saturation shift referencing (WASSR) for chemical exchange saturation transfer (CEST) experiments. Magn Reson Med 2009;61(6):1441–50.
[49] Togao O, Keupp J, Hiwatashi A, Yamashita K, Kikuchi K, Yoneyama M, et al. Amide proton transfer imaging of brain tumors using a self-corrected 3D fast spin-echo dixon method: comparison with separate B(0) correction. Magn Reson Med 2017;77(6):2272–9.
[50] Sacolick LI, Wiesinger F, Hancu I, Vogel MW. B1 mapping by Bloch-Siegert shift. Magn Reson Med 2010;63(5):1315–22.
[51] Schuenke P, Windschuh J, Roeloffs V, Ladd ME, Bachert P, Zaiss M. Simultaneous mapping of water shift and B(1) (WASABI)-application to field-inhomogeneity correction of CEST MRI data. Magn Reson Med 2017;77(2):571–80.
[52] Windschuh J, Zaiss M, Meissner JE, Paech D, Radbruch A, Ladd ME, et al. Correction of B1-inhomogeneities for relaxation-compensated CEST imaging at 7T. NMR Biomed 2015;28(5):529–37.
[53] Cember ATJ, Hariharan H, Kumar D, Nanga RPR, Reddy R. Improved method for post-processing correction of B(1) inhomogeneity in glutamate-weighted CEST images of the human brain. NMR Biomed 2021;34(6):e4503.
[54] Liebert A, Zaiss M, Gumbrecht R, Tkotz K, Linz P, Schmitt B, et al. Multiple interleaved mode saturation (MIMOSA) for B(1)(+) inhomogeneity mitigation in chemical exchange saturation transfer. Magn Reson Med 2019;82(2):693–705.
[55] Singh A, Cai K, Haris M, Hariharan H, Reddy R. On B1 inhomogeneity correction of in vivo human brain glutamate chemical exchange saturation transfer contrast at 7T. Magn Reson Med 2013;69(3):818–24.
[56] Khlebnikov V, Windschuh J, Siero JC, Zaiss M, Luijten PR, Klomp DW, et al. On the transmit field inhomogeneity correction of relaxation-compensated amide and NOE CEST effects at 7 T. NMR Biomed 2017;30(5).
[57] Poblador Rodriguez E, Moser P, Auno S, Eckstein K, Dymerska B, van der Kouwe A, et al. Real-time motion and retrospective coil sensitivity correction for CEST using volumetric navigators (vNavs) at 7T. Magn Reson Med 2021;85(4): 1909–23.
[58] Stabinska J, Müller-Lutz A, Wittsack HJ, Tell C, Rump LC, Ertas N, et al. Two point Dixon-based chemical exchange saturation transfer (CEST) MRI in renal transplant patients on 3 T. Magn Reson Imaging 2022;90:61–9.
[59] Wu B, Jia F, Li X, Zhang M, Han D, Jia Z. Amide proton transfer imaging vs diffusion kurtosis imaging for predicting histological grade of hepatocellular carcinoma. J Hepatocell Carcinoma 2020;7:159–68.
[60] Lin Y, Luo X, Yu L, Zhang Y, Zhou J, Jiang Y, et al. Amide proton transfer-weighted MRI for predicting histological grade of hepatocellular carcinoma: comparison with diffusion-weighted imaging. Quant Imaging Med Surg 2019;9 (10):1641–51.
[61] Wu B, Jia F, Li X, Li L, Wang K, Han D. Comparative study of amide proton transfer imaging and intravoxel incoherent motion imaging for predicting histologic grade of hepatocellular carcinoma. Front Oncol 2020;10:562049.
[62] Jia X, Wang W, Liang J, Ma X, Chen W, Wu D, et al. Risk stratification of abdominal tumors in children with amide proton transfer imaging. Eur Radiol 2022;32(4):2158–67.
[63] Lindquist DM, Fugate EM, Wang J, Sharma A, Gandhi CR, Dillman JR. MRI measures of murine liver fibrosis. J Magn Reson Imaging 2021;54(3):739–49.
[64] Maloney E, Wang YN, Vohra R, Son H, Whang S, Khokhlova T, et al. Magnetic resonance imaging biomarkers for pulsed focused ultrasound treatment of pancreatic ductal adenocarcinoma. World J Gastroenterol 2020;26(9):904–17.
[65] Vohra R, Wang YN, Son H, Totten S, Arora A, Maxwell A, et al. Non-invasive monitoring of increased fibrotic tissue and hyaluronan deposition in the tumor microenvironment in the advanced stages of pancreatic ductal adenocarcinoma. Cancers (Basel) 2022;14(4).
[66] Nishie A, Asayama Y, Ishigami K, Ushijima Y, Takayama Y, Okamoto D, et al. Amide proton transfer imaging to predict tumor response to neoadjuvant chemotherapy in locally advanced rectal cancer. J Gastroenterol Hepatol 2019;34 (1):140–6.
[67] Chen W, Mao L, Li L, Wei Q, Hu S, Ye Y, et al. Predicting treatment response of neoadjuvant chemoradiotherapy in locally advanced rectal cancer using amide proton transfer MRI combined with diffusion-weighted imaging. Front Oncol 2021;11:698427.
[68] Suzuki A, Maeda T, Baba Y, Shimamura K, Kato Y. Acidic extracellular pH promotes epithelial mesenchymal transition in Lewis lung carcinoma model. Cancer Cell Int 2014;14(1):129.
[69] Chand M, Yu S, Swift RI, Brown G. Mucinous carcinoma of the rectum: a distinct clinicopathological entity. Tech Coloproctol 2014;18(4):335–44.
[70] Li L, Chen W, Yan Z, Feng J, Hu S, Liu B, et al. Comparative analysis of amide proton transfer MRI and diffusion-weighted imaging in assessing p53 and Ki-67 expression of rectal adenocarcinoma. J Magn Reson Imaging 2020;52(5): 1487–96.
[71] Chen W, Li L, Yan Z, Hu S, Feng J, Liu G, et al. Three-dimension amide proton transfer MRI of rectal adenocarcinoma: correlation with pathologic prognostic factors and comparison with diffusion kurtosis imaging. Eur Radiol 2021;31(5): 3286–96.
[72] Li J, Lin L, Gao X, Li S, Cheng J. Amide proton transfer weighted and intravoxel incoherent motion imaging in evaluation of prognostic factors for rectal adenocarcinoma. Front Oncol 2021;11:783544.
[73] Ju Y, Liu A, Wang Y, Chen L, Wang N, Bu X, et al. Amide proton transfer magnetic resonance imaging to evaluate renal impairment in patients with chronic kidney disease. Magn Reson Imaging 2022;87:177–82.
[74] Yin H, Wang D, Yan R, Jin X, Hu Y, Zhai Z, et al. Comparison of diffusion kurtosis imaging and amide proton transfer imaging in the diagnosis and risk assessment of prostate cancer. Front Oncol 2021;11:640906.
[75] Jia G, Abaza R, Williams JD, Zynger DL, Zhou J, Shah ZK, et al. Amide proton transfer MR imaging of prostate cancer: a preliminary study. J Magn Reson Imaging 2011;33(3):647–54.
[76] Yang L, Wang L, Tan Y, Dan H, Xian P, Zhang Y, et al. Amide proton transfer-weighted MRI combined with serum prostate-specific antigen levels for differentiating malignant prostate lesions from benign prostate lesions: a retrospective cohort study. Cancer Imaging 2023;23(1):3.
[77] Qin X, Mu R, Zheng W, Li X, Liu F, Zhuang Z, et al. Comparison and combination of amide proton transfer magnetic resonance imaging and the apparent diffusion coefficient in differentiating the grades of prostate cancer. Quant Imaging Med Surg 2023;13(2):812–24.
[78] Hu W, Chen L, Lin L, Wang J, Wang N, Liu A. Three-dimensional amide proton transfer-weighted and intravoxel incoherent motion imaging for predicting bone metastasis in patients with prostate cancer: a pilot study. Magn Reson Imaging 2023;96:8–16.
[79] Ishimatsu K, Nishie A, Takayama Y, Asayama Y, Ushijima Y, Kakihara D, et al. Amide proton transfer imaging for differentiating benign ovarian cystic lesions: potential of first time right. Eur J Radiol 2019;120:108656.
[80] Li Y, Lu X, Chen L, Zhang Q, Wang N, Wang J, et al. Identification of ovarian endometriotic cysts in cystic lesions of the ovary by amide proton transfer-weighted imaging and R2* mapping. Clin Radiol 2023;78(2) (e106-e12).
[81] Yu Y, Song X, Zeng Z, Wang L, Zhang L, Zhao H, et al. Amide proton transfer weighted MRI in differential diagnosis of ovarian masses with cystic components: a preliminary study. Magn Reson Imaging 2023;103:216–23.
[82] Li S, Liu J, Zhang Z, Wang W, Lu H, Lin L, et al. Added-value of 3D amide proton transfer MRI in assessing prognostic factors of cervical cancer: a comparative study with multiple model diffusion-weighted imaging. Quant Imaging Med Surg 2023;13(12):8157–72.
[83] Meng N, Wang J, Sun J, Liu W, Wang X, Yan M, et al. Using amide proton transfer to identify cervical squamous carcinoma/adenocarcinoma and evaluate its differentiation grade. Magn Reson Imaging 2019;61:9–15.
[84] Li B, Sun H, Zhang S, Wang X, Guo Q. Amide proton transfer imaging to evaluate the grading of squamous cell carcinoma of the cervix: a comparative study using (18) F FDG PET. J Magn Reson Imaging 2019;50(1):261–8.
[85] Hou M, Song K, Ren J, Wang K, Guo J, Niu Y, et al. Comparative analysis of the value of amide proton transfer-weighted imaging and diffusion kurtosis imaging in evaluating the histological grade of cervical squamous carcinoma. BMC Cancer 2022;22(1):87.
[86] Xu Q, Song Q, Wang Y, Lin L, Tian S, Wang N, et al. Amide proton transfer weighted combined with diffusion kurtosis imaging for predicting lymph node metastasis in cervical cancer. Magn Reson Imaging 2023;106:85–90.

[87] Zhang S, Sun H, Li B, Wang X, Pan S, Guo Q. Variation of amide proton transfer signal intensity and apparent diffusion coefficient values among phases of the menstrual cycle in the normal uterus: a preliminary study. Magn Reson Imaging 2019;63:21–8.
[88] Li Y, Lin CY, Qi YF, Wang XQ, Chen B, Zhou HL, et al. Non-invasive differentiation of endometrial adenocarcinoma from benign lesions in the uterus by utilization of amide proton transfer-weighted MRI. Mol Imaging Biol 2021;23 (3):446–55.
[89] Li Y, Lin CY, Qi YF, Wang X, Chen B, Zhou HL, et al. Three-dimensional turbo-spin-echo amide proton transfer-weighted and intravoxel incoherent motion MR imaging for type I endometrial carcinoma: correlation with Ki-67 proliferation status. Magn Reson Imaging 2021;78:18–24.
[90] Shifeng T, Yue W, Wen Z, Lihua C, Nan W, Liangjie L, et al. The value of multimodal functional magnetic resonance imaging in differentiating p53abn from p53wt endometrial carcinoma. Acta Radiol 2023;64(11):2948–56.
[91] Li X, Tian S, Ma C, Chen L, Qin J, Wang N, et al. Multimodal MRI for estimating Her-2 gene expression in endometrial cancer. Bioeng (Basel, Switzerland) 2023; vol. 10(12).
[92] Li Y, Liu X, Wang X, Lin C, Qi Y, Chen B, et al. Using amide proton transfer-weighted MRI to non-invasively differentiate mismatch repair deficient and proficient tumors in endometrioid endometrial adenocarcinoma. Insights Imaging 2021;12(1):182.
[93] Meng N, Fang T, Feng P, Huang Z, Sun J, Wang X, et al. Amide proton transfer-weighted imaging and multiple models diffusion-weighted imaging facilitates preoperative risk stratification of early-stage endometrial carcinoma. J Magn Reson Imaging 2021;54(4):1200–11.
[94] Fu F, Meng N, Huang Z, Sun J, Wang X, Shang J, et al. Identification of histological features of endometrioid adenocarcinoma based on amide proton transfer-weighted imaging and multimodel diffusion-weighted imaging. Quant Imaging Med Surg 2022;12(2):1311–23.
[95] Ochiai R, Mukuda N, Yunaga H, Kitao S, Okuda K, Sato S, et al. Amide proton transfer imaging in differentiation of type II and type I endometrial carcinoma: a pilot study. Jpn J Radiol 2022;40(2):184–91.
[96] Tian S, Chen A, Li Y, Wang N, Ma C, Lin L, et al. The combined application of amide proton transfer imaging and diffusion kurtosis imaging for differentiating stage Ia endometrial carcinoma and endometrial polyps. Magn Reson Imaging 2023;99:67–72.
[97] Meng X, Tian S, Zhang Q, Chen L, Lin L, Li J, et al. Improved differentiation between stage I-II endometrial carcinoma and endometrial polyp with combination of APTw and IVIM MR imaging. Magn Reson Imaging 2023;102: 43–8.
[98] Ma C, Tian S, Song Q, Chen L, Meng X, Wang N, et al. Amide proton transfer-weighted imaging combined with intravoxel incoherent motion for evaluating microsatellite instability in endometrial cancer. J Magn Reson Imaging 2023;57 (2):493–505.
[99] Jin X, Yan R, Li Z, Zhang G, Liu W, Wang H, et al. Evaluation of amide proton transfer-weighted imaging for risk factors in stage I endometrial cancer: a comparison with diffusion-weighted imaging and diffusion kurtosis imaging. Front Oncol 2022;12:876120.
[100] Zhou J, Hong X, Zhao X, Gao JH, Yuan J. APT-weighted and NOE-weighted image contrasts in glioma with different RF saturation powers based on magnetization transfer ratio asymmetry analyses. Magn Reson Med 2013;70(2):320–7.